


## Loss-Compensated and Enhanced Midinfrared Interaction-Free Sensing with Undetected Photons

Nathan R. Gemmell,<sup>1,\*</sup> Jefferson Flórez,<sup>1</sup> Emma Pearce,<sup>1</sup> Olaf Czerwinski,<sup>1</sup> Chris C. Phillips,<sup>1</sup> Rupert F. Oulton,<sup>1</sup> and Alex S. Clark<sup>1,2</sup>

<sup>1</sup>*Department of Physics, Blackett Laboratory, Imperial College London, South Kensington Campus, London SW7 2AZ, United Kingdom*

<sup>2</sup>*Quantum Engineering Technology Labs, H. H. Wills Physics Laboratory and Department of Electrical and Electronic Engineering, University of Bristol, Bristol BS8 1FD, United Kingdom*

 (Received 23 September 2022; revised 16 February 2023; accepted 21 March 2023; published 5 May 2023)

Sensing with undetected photons enables the measurement of absorption and phase shifts at wavelengths different from those detected. Here, we experimentally map the balance and loss parameter space in a nondegenerate nonlinear interferometer, showing the recovery of sensitivity despite internal losses at the detection wavelength. We further explore an interaction-free operation mode with a detector-to-sample incident optical power ratio of over 200. This allows changes in attowatt levels of power at 3.4  $\mu\text{m}$  wavelength to be detected at 1550 nm, immune to the level of thermal black-body background. This reveals an ultrasensitive infrared imaging methodology capable of probing samples effectively “in the dark.”

DOI: [10.1103/PhysRevApplied.19.054019](https://doi.org/10.1103/PhysRevApplied.19.054019)

### I. INTRODUCTION

Induced coherence without induced emission was demonstrated experimentally by Zou, Wang, and Mandel in 1991 [1], where interference was observed between the down-converted photons generated in two separate nonlinear crystals. It was shown that the interference was dependent on the mutual indistinguishability of the two crystals' signal and idler fields; any distinguishability introduced between the idler fields, for example, reduced the visibility of interference between the signal beams at the detector [2]. Remarkably, this allows information about an object probed by one idler beam to be gained only from measuring the interference between the signal beams. While an initial demonstration of an application of induced coherence was for spectroscopy [3], its application to imaging has since caused a significant pique in interest [4]. This technique does not rely on up-conversion [5,6] (which is often inefficient and can introduce spurious background noise) or indeed any detection capability at the probe wavelength, as is necessary for nondegenerate “ghost imaging” [7,8]. The primary attraction to the

sensing community is clear: infrared sensing capability using significantly cheaper, lower noise, and more readily available visible photon detection technology. This capability has dramatic consequences in the field of midinfrared sensing where not only is imaging technology limited, but the thermal black-body background plays a significant role in the achievable signal-to-noise ratio (SNR). With induced coherence-based midinfrared sensing, background thermal noise only contributes at the signal wavelength, where it can be considered irrelevant for room temperature samples.

Much effort in recent years in the field of induced coherence has involved simplifying the methodology and apparatus to make the technique more accessible. This has resulted in the implementation of “folded” systems which use a double pass of a single nonlinear crystal [9–18], seeded versions of the experiment [19,20], an interferometer that uses two different nonlinear processes [21], spectroscopy based on all fields passing stacked crystals [22], as well as spectroscopy using a seeding source [23]. This work continues to push the technology closer to real-world applications [24], though for full applicability one needs to compare to the features of current imaging capabilities and limits. The dynamic range of an imaging system can be defined as the ratio between the maximum and minimum possible intensity values. Furthermore, typical imaging systems have a feature whereby the intensity ( $I$ ) measured at pixels can be mapped to stored values ( $V$ ) via a power law  $V = CI^\gamma$ , where  $\gamma$  is a correction factor

\*n.gemmell20@imperial.ac.uk

*Published by the American Physical Society under the terms of the [Creative Commons Attribution 4.0 International](https://creativecommons.org/licenses/by/4.0/) license. Further distribution of this work must maintain attribution to the author(s) and the published article's title, journal citation, and DOI.*

used to store images in a manner closer to how our eyes perceive light ( $C$  is a constant of conversion). However, for systems based on induced coherence the dynamic range and  $\gamma$  are dependent on the physical processes involved. The dynamic range of the undetected imaging system will be set and controlled by the visibility range of the nonlinear interference and not by the physical dynamic range of the camera used (due to the well depth of the pixels and bit depth of the analogue-to-digital conversion), while  $\gamma$  is defined by the relationship between the sample transmissivity in the idler arm and interference visibility. One approach to tuning this relationship is operating in the so-called “high-gain” regime, where pump powers are high enough for the down-conversion process to self-seed [25]. In this way, the interferometer’s visibility range can be maximized over the transmissivity range of the relevant sample. This method also provides greater phase sensitivity [25,26]. Reaching a regime to see significant tunability of the dynamic range, however, requires operation with levels of power that are impractical for some imaging systems, not discounting the limitations of pump depletion [27]. Even in the low-gain regime, the balance of photon numbers generated in the two processes of a nonlinear interferometer is central to maximizing the dynamic range for imaging with undetected photons [20].

Imaging systems based on induced coherence are also ideal for photosensitive samples as the object need only be interrogated by the idler beam from the first process while the detector sees the induced coherence via signal beam photons from two. This leads to an effect akin to “interaction-free imaging” [28,29], where there can be a discrepancy between the optical power impinging on the sample and that which hits the detector (since the detected photons do not interact with the sample). In the case of a nondegenerate nonlinear interferometer, this effect is enhanced due to the mismatch in the signal and idler wavelengths (where the beam that probes a sample has a significantly lower photon energy and is therefore inherently less photodamaging). This power discrepancy seen between sample and detector can be enhanced even further by unbalancing the interferometer, such that even fewer photons are generated in the path that interacts with the sample. Again, careful balancing of the interferometer is important to maintain detectable interference visibility.

In this work, we study the balance of power in nonlinear interferometers both theoretically and experimentally. We show that losses of the first signal beam within the interferometer can be compensated for and that the “interaction-free” effect can be exploited. This could have significant implications for the design of future nonlinear interferometers, particularly those based on “folded” designs where redressing the balance of the system is more difficult, or those designed for probing ultraphotosensitive samples.

## II. THEORY

We restrict our theoretical analysis only to the Michelson “folded” design. In such an interferometer, a single nonlinear crystal is pumped in one direction, generating the first signal and idler fields at wavelengths  $\lambda_s$  and  $\lambda_i$ . These are subsequently reflected back through the crystal with a second pump (most commonly the first pump reflected), generating the second signal and idler fields necessary for the induced coherence. Such a system can be comprehensively modeled using the theory presented by Giese *et al.* [26], and it is this framework we use to analyze our system. We consider the assumptions of a monochromatic plane-wave pump beam applicable to the experimental system presented below, given the linewidth of our pump laser and optical geometry of the system. We also restrict any analysis to the nondegenerate case since this is where the majority of interest lies for practical imaging applications, making use of the transfer of information between wavelengths. Further, since detector losses merely act as a multiplying term, we omit them here. A schematic of the model is shown in Fig. 1, where A and B in this case denote the first and second passes of the same nonlinear crystal. From this treatment, it can be shown that the number of photons incident on the signal detector can be expressed as

$$N_\phi(r) = T_s G_A + G_B + (T_s + T_i(r)) G_A G_B - 2\sqrt{T_s T_i(r)(1 + G_A)(1 + G_B) G_A G_B} \cos \phi, \quad (1)$$

where  $T_s$  and  $T_i(r)$  are the transmissivities of the paths of the first signal and idler fields to the second crystal, respectively (note that the transmission of the idler has a transverse position dependency relating to an object placed in the idler arm), and  $G_A$  and  $G_B$  represent hyperbolic functions defining the nonlinear gain parameters for the nonlinear crystals A and B [proportional to the input power via  $G_x \propto \sinh^2(\sqrt{P_x})$  where  $x \in \{A, B\}$ ]. The parameter  $\phi = \phi_p - \phi_i - \phi_s$  represents the total accumulated phase shift between the secondary pump and the primary signal and idler fields, respectively. Using Eq. (1), we can now model a nonlinear interferometer for arbitrary losses in the signal and idler beams, as well as for uneven gain parameters in the two crystals, due to unbalanced pumping powers.

In the low-gain regime tested here, where  $G_{A,B} \ll 1$ , it is worth noting that the number of photons can be simplified to:

$$N_\phi(r) = T_s G_A + G_B - 2\sqrt{T_s T_i(r) G_A G_B} \cos \phi, \quad (2)$$

since the terms relating to any seeding processes of crystal B from crystal A have a negligible contribution. The performance of nonlinear interferometers can be defined using two parameters: the amplitude and visibility of the interference fringes. The amplitude can be simply defined as the

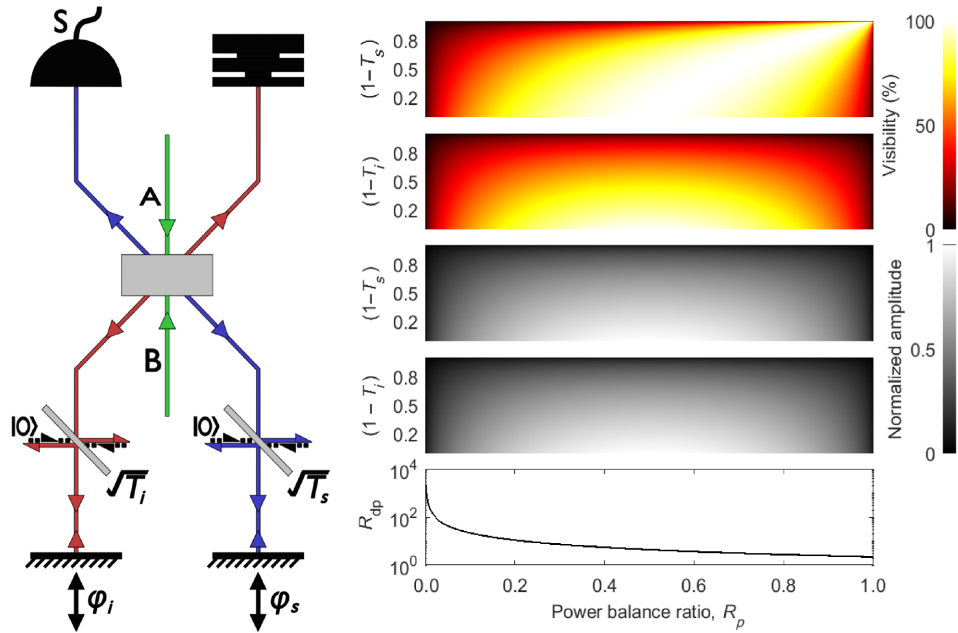


FIG. 1. Left: Schematic of theoretical model of a nondegenerate nonlinear interferometer. Green indicates the pump beam, blue and red represent signal and idler beams, respectively. Process A is unseeded. Detection takes place on the signal beam after reflection and return through the nonlinear process overlapping with pump B and the reflected idler beam. The output idler photons are discarded. Losses are modeled as beam splitters with transmissivity  $\sqrt{T_{s,i}}$ , such that total transmissivity of the beam is  $T_{s,i}$ . Phase shifts ( $\phi_{s,i}$ ) are introduced on reflection. Right: Visibility ( $\mathcal{V}$ ) and amplitude ( $\mathcal{A}$ ) (normalized to input power) of the interference as a function of both internal signal or idler loss ( $1 - T_{s,i}$ ) on the  $y$  axis and power balance ratio ( $R_p$ ) on the  $x$  axis. The bottom plot shows the detection-to-probe power ratio  $R_{dp}$ .

difference between the numbers of photons detected at the peak of the fringe (at  $\phi_{\max}$ ) and at the trough (at  $\phi_{\max} + \pi$ ) such that  $\mathcal{A}(r) = N_{\phi_{\max}}(r) - N_{\phi_{\max} + \pi}(r)$ . The visibility of the interference fringes,  $\mathcal{V}(r)$ , is defined as the amplitude normalized by the sum of photon numbers at the peak and trough,

$$\mathcal{V}(r) = \frac{\mathcal{A}(r)}{(N_{\phi_{\max}}(r) + N_{\phi_{\max} + \pi}(r))}. \quad (3)$$

From here it can be shown that if we define  $\mathcal{V}_0$  as the visibility of the system with  $T_i(r) = 1$ , then, using Eq. (2), the visibility can be shown to relate to the transmission of the idler arm by

$$\mathcal{V}(r) = \sqrt{T_i(r)} \mathcal{V}_0, \quad (4)$$

such that a measurement of the transverse position-dependent visibility of the signal maps out an image of the transmissivity of the sample in the idler arm.

In assessing the practicality of these systems as mentioned above, one can also measure the ‘‘interaction-free’’ efficiency, simply defined as the number of photons incident on the detector over the number of photons incident on the sample (akin to the amplification factor defined in [15]). However, in a nondegenerate regime such as that discussed here there is also the energy discrepancy between

the signal and idler photons, leading to a further power unbalancing between the detected and probe light beams. This can then be defined as the detection-to-probe power ratio

$$R_{dp} = \frac{N_d \lambda_i}{N_s \lambda_s}, \quad (5)$$

where  $N_d$  and  $N_s$  are the average number of photons incident on the detector and sample, respectively. The effects of power balance (ratio of input power to first and second nonlinear processes) and first signal beam transmission,  $T_s$ , on visibility and amplitude, are shown on the right in Fig. 1, along with a plot showing the detection-to-probe power ratio. The power balance  $R_p$  used on the  $x$  axis of these maps assumes a constant input power into the interferometer, which can be distributed arbitrarily between the two passes of the crystal and is simply calculated as the ratio of input power sent to the first pass to the total input power. All remaining power is assumed to be used in the second pass with no loss.

The top map shows the possibility of regaining high visibility, even in the presence of high loss of the first signal beam, by simply directing more power to the first nonlinear process, as shown by the asymmetry. This can be intuitively interpreted by considering that an equal probability

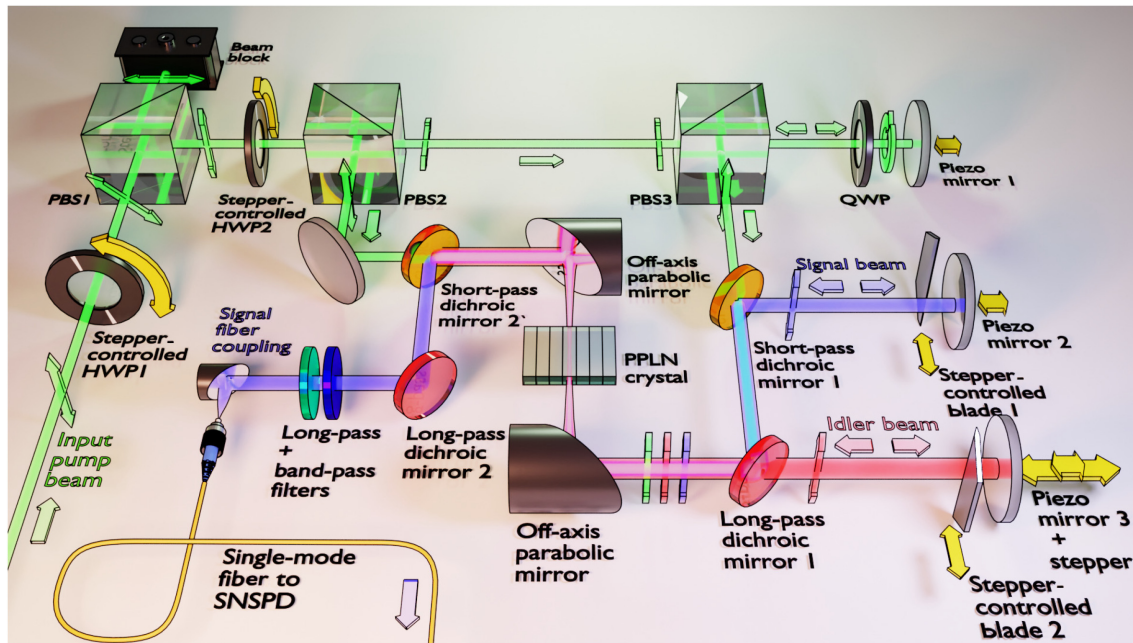


FIG. 2. Schematic of experimental setup. Green beam paths indicate pump (1064 nm), blue represents the signal paths (1550 nm), and red corresponds to the idler (3.4  $\mu\text{m}$ ). Yellow arrows indicate automated translation.

of detecting a photon from either arm yields maximum visibility. However, as shown in the corresponding amplitude plot, sending more of the available power to the first process to maximize visibility comes at the expense of the amplitude of the interference fringes, as it will significantly reduce the amount of detectable signal. Unbalancing in the opposite direction (more power to the second process) dramatically increases the detection-to-probe power ratio, though this will always come at the expense of both amplitude and visibility. Losses in the first idler always result in a reduction of both signal and visibility and cannot be redressed with an unbalancing of pumps (within the low-gain regime tested experimentally here, as defined above), since this loss in the idler does not represent a change in the balance of signal photons generated in the first and second nonlinear processes.

### III. EXPERIMENTAL PROCEDURE

Figure 2 shows a schematic of the unbalanced nonlinear interferometer designed to test this theory. The input power of the pump beam (1064 nm Azurlight continuous wave attenuated to approximately 1 mW) is adjusted via reflection from a polarizing beam splitter (PBS 1) after passing a half-wave plate (whose angle is computer-controlled by a servo motor, HWP 1). The pump beam is then split into two arms via a second PBS (PBS 2), that defines the two pump beams for the interferometer. The balance of power between the two pump processes can then be adjusted via a second servo-controlled half-wave

plate (HWP 2), without changing the total power input to the system. This also allows an experimental study of the regime in which the spontaneous parametric gain of the second process is higher than that of the first, something only previously studied with a two-crystal setup and a difference in phase-matching conditions [30].

The second pump arm is sent through another PBS (PBS 3) and a quarter-wave plate (QWP) before being reflected from a mirror to double pass the QWP, rotating the polarization to vertical and exiting the reflection port of the PBS. This reflection scheme enables the second pump phase to be adjusted by a computer-controlled piezoelectric motor (piezo mirror 1).

The nonlinear crystal is a temperature-controlled periodically poled lithium niobate (PPLN) chip supplied by Covision, with a poling period of  $\Lambda = 30.5 \mu\text{m}$ , and antireflection coated to  $R < 1.5\%$  at 1064 nm, to  $R < 1\%$  between 1400 and 1800 nm, and to  $R$  from about 6% to 3% between 2600 nm and 4800 nm, on both input and output facets. Both pump beams are weakly focused into either facet of the crystal through silver off-axis parabolic mirrors with focal length 152 mm (resulting in a 0.12-mm  $1/e^2$  pump beam waist). These mirrors also serve to collect and collimate the generated signal and idler photons from both pumping directions. Signal and idlers from the primary pump pass are tapped off from the pump beam via two dichroic mirrors [1180-nm short-pass from Thorlabs (short-pass dichroic mirror 1) and 2100-nm long-pass from Layertec (long-pass dichroic mirror 1), respectively], and sent to two mirrors with computer-controlled piezo-motor

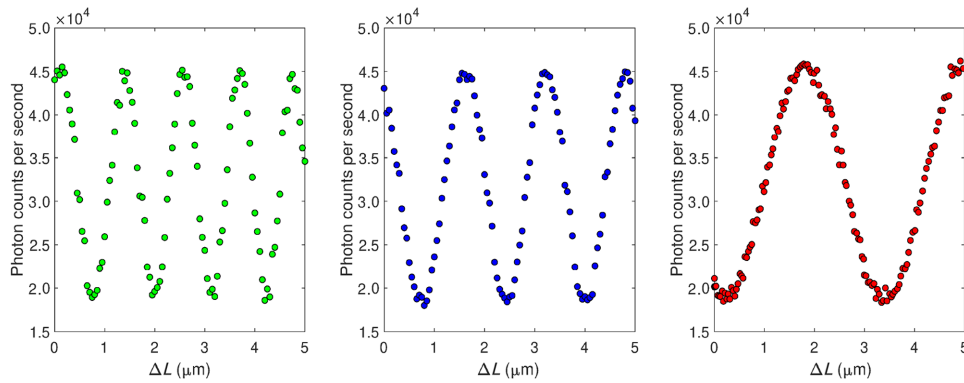


FIG. 3. Signal count rates as a function of the length change  $\Delta L$  in the secondary pump path (left, green), internal signal path (middle, blue), and internal idler path (right, red).

positioning which reflect the beams back through the crystal with an accumulated phase shift from the piezo motor (piezo mirrors 2 and 3). The idler mirror has an additional computer-controlled translation stage (stepper motor) to enable the path length between signal and idler photons to be matched. Two independent computer-controlled translation stages (stepper motors) adjust the positions of knife blades in the first signal and idler beams, allowing arbitrary amounts of loss to be introduced into each arm. Spontaneous parametric down-conversion photons generated from the first pump returning through the crystal overlap with those generated from the second pump beam, with the signal photons subsequently being isolated via a second 1180-nm short-pass dichroic (short-pass dichroic mirror 2). The signal photons are then filtered [2100-nm long-pass from Layertec (long-pass dichroic mirror 2), and 12-nm wide 1550-nm bandpass and 1400-nm long-pass, from Thorlabs], coupled into standard telecommunications single-mode fiber (SMF-28) and sent to a superconducting nanowire single-photon detector (SNSPD, IDQuantique, approximately 80% detection efficiency at 1550 nm), where count rates are monitored by a pulse counting module (ID900) with a 50-ms acquisition time.

#### IV. RESULTS

Figure 3 shows the fluctuation of single-photon signal beam counts as a function of the phase shift introduced by the piezo mirrors in the second pump, the signal, and the idler beams. As each piezo motor is scanned, the signal count rate oscillates with a period of the wavelength of the scanned field (1064 nm for the pump, 1550 nm for the signal, and 3390 nm for the idler). The idler piezo motor has a strain gauge (unlike the signal and pump piezos) which ensures that errors in the piezo position due to hysteresis can be monitored and corrected, and thus the idler wavelength can be measured to higher precision. For the

rest of the results presented in this paper, it was the idler field that was scanned. Experimental results on how the visibility and amplitude of the interference fringes change as a function of power balance (half-wave plate angle) and first signal beam losses (introduced by the knife-blade position) are shown in the left panels of Fig. 4. Each data point of visibility was extracted from a fit to a sine wave for data taken such as that shown in the right panel of Fig. 3, where the idler phase has been scanned. Due to an overestimation of the visibility at very low count rates—resulting from a highly varying noise floor—the visibility was clamped to zero in cases where the SNR was less than 1; this gives rise to the sharp edges seen in the experimental data plots. The SNR was calculated from the visibility goodness of fit. As is immediately evident, the high visibility cannot be maintained at high losses, even at extreme power unbalancing, due to the reduced SNR as a result of fewer signal photon counts. In the experimental visibility plot (top left) there is a distinct asymmetry in the data as seen in the theory presented in the top right panel of Fig. 1. Indeed, using this theory and entering realistic numbers for fixed losses (6% loss each way from crystal facets, 3% loss each way from the parabolic mirror, 2% loss each way from the dichroic mirror, and 4% loss from the plano retroreflecting mirror), beam diameters, beam-splitter extinction ratios, and background counts (0.01 Hz) yields the theoretical results presented in the right panel of Fig. 4. The match between theory and experiment in shape and visibility is only reached with an additional 60% loss to the first idler beam.

This match between theory and experiment confirms the validity of the model, though higher initial experimental fringe visibility would allow for regimes of even higher signal losses to be probed, and better SNR in an image. It is also worth noting that the spatial resolution of an imaging system based on this technique would correlate to the strength of signal-idler correlations (in either position or momentum), and thus not have a bearing on the visibility

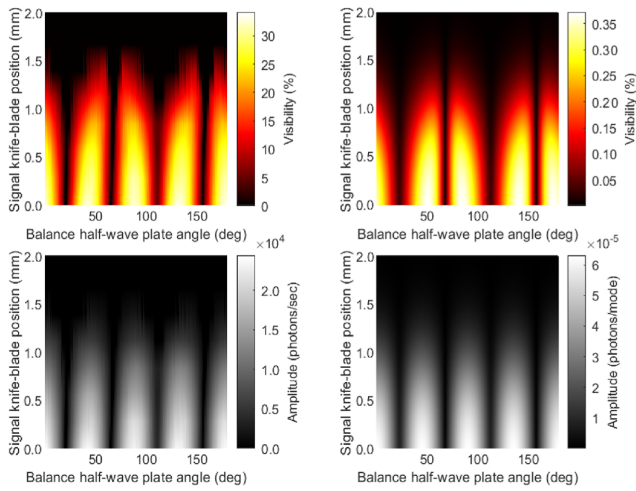


FIG. 4. Left: Experimental data showing the visibility (top) and amplitude (bottom) of the interference fringes as a function of both power balance between the two crystals (adjusted via half-wave plate angle,  $x$  axis), and primary signal loss (introduced via a stepper-mounted knife blade, position marked by  $y$  axis). Right: A theoretical model of experimental design.

[31–33]. Figure 5 shows the same plots as Fig. 4, but for varying internal idler losses (position of the knife blade in the idler beam). As predicted by the model, the data show no sign of the asymmetry present when there is high first signal beam loss. Again, data fitted with an SNR less than 1 have been clamped to zero to mitigate overfitting visibility values at low SNR. The symmetry shown in this plot confirms that the low maximum visibility observed in this system is not due to first signal beam losses, but instead may be due to high first idler beam loss. This reduction in visibility due to what is described as “loss” in the model is difficult to quantify experimentally without the ability to detect the idler wavelength. However, it should be noted that visibility is reduced by any introduced distinguishability on the idler; for example, misalignment of the returning idler with the secondary pump axis, optical aberrations within the setup (the off-axis parabolic mirrors may be introducing some comatic aberration), any rotation of polarization of the idler photon, or clipping of the idler beam through the system (due to the phase matching conditions, the idler beam width is larger than that of the signal or pump). While all or any of these may be contributing to the “losses” in our system, with no way to detect the photons, quantifying them remains out of reach.

The data presented in Fig. 5 represent how typical ‘imaging with undetected photons’ systems operate, where losses in the idler arm are mapped to changes in the visibility of the interference fringes of the signal photons. Thus, when a change in visibility (or phase) is measured at a pixel in such an imaging system it can be converted into a transmissivity (or phase shift) at that position. An

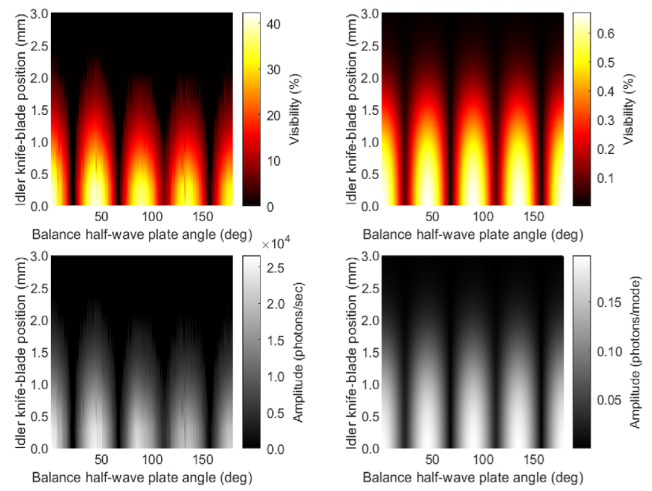


FIG. 5. Left: Experimental data showing the visibility (top) and amplitude (bottom) of the interference fringes as a function of both power balance between the two crystals (adjusted via half-wave plate angle,  $x$  axis), and primary idler loss (introduced via a stepper-mounted knife blade, position marked by  $y$  axis). Right: A theoretical model of experimental design.

obvious interpretation of these results is that perfect balancing gives the optimal performance for this kind of imaging system. However, such a conclusion would ignore the advantages of the aforementioned “interaction-free” operation. As stated in Sec. II, such a discrepancy in the probing and detection optical powers offers the opportunity to observe delicate processes in far greater detail than ever before. Figure 6 demonstrates this principle. With the balancing half-wave plate set at 44°, the visibility is at its peak and shows well the reduction with respect to losses (position of the knife blade). While the visibility has been severely reduced at a half-wave plate angle of 25°, the ratio of detected-to-probing power has increased by a factor greater than 40 to over 200 (for a power balance ratio  $R_p$  of 0.01). This means that for every nanowatt of power detected the sample can be exposed to less than 5 pW of illumination power (compared to 205 pW at 45°). For the data presented here, the average signal count rate is  $3 \times 10^4$  cps, corresponding to 3.8 fW, giving the power incident on the sample at a balance half-wave plate position of 25° as 18.7 aW. While there are emerging ways to detect single photons in this region of the spectrum [34,35], their single-photon detection or conversion efficiency remains low (0.1%–2%), while noise from background sources may increase. Such detection systems currently would provide no significant gains in simplifying the optical setup, and instead would be incapable of reaching the sensitivities achieved here. Predictions of 2%–50% system detection efficiency capability for SNSPDs working up to 10- $\mu$ m wavelengths have been put forward [36,37], but not yet demonstrated.

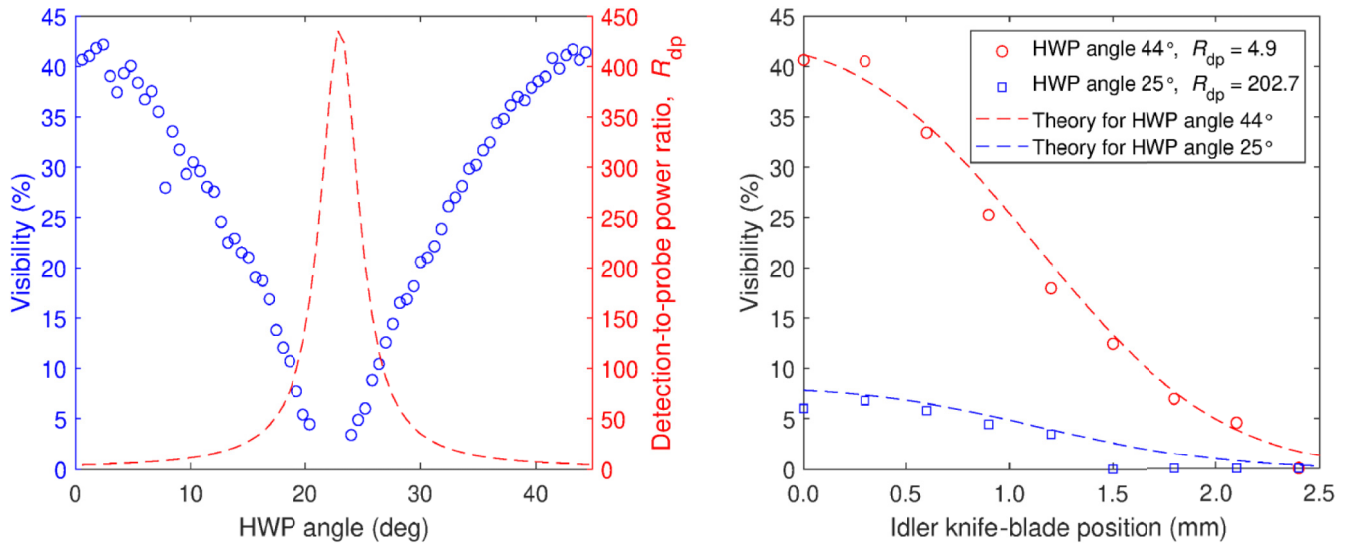


FIG. 6. Left: Visibility without knife-blade losses (left axis, blue circles) and detection-to-probe power ratio,  $R_{dp}$ , plotted as a function of balance half-wave plate angle (right axis, red dashed line). Right: Visibility plotted as a function of losses in the primary idler arm for two different half-wave plate positions: 44° (red circles) and 25° (blue squares). Lines show the theoretical model.

## V. CONCLUSIONS

We have shown that the balance of pump power in a nonlinear interferometer can be used to improve interference visibility in the presence of loss of the first signal beam. The result of this interplay of interferometer balancing and losses is key to understanding and implementing real-world imaging systems based on nonlinear interferometry. Furthermore, we have demonstrated that an imbalance can also be purposefully introduced at the expense of visibility to maximize the power unbalance in the probing and detecting beams. This allows a sample to be illuminated with fewer photons and significantly lower power than that detected, resulting in an ultralow power imaging methodology. Such a situation allows the construction of imaging systems capable of probing samples effectively “in the dark” which could include photosensitive molecules (where photobleaching of molecules will reduce the ability to detect them [38]), biological samples [where light can cause cellular damage (i.e., phototoxicity [39,40]), or where one could study live light-sensitive cells in their “off” state without using fluorescent markers [41]], or historical artifacts (where hidden layers can usually only be revealed by optical powers which cause damage [16]). This technique opens the door to the possibility of imaging in the midinfrared far below the noise floor of current midinfrared camera technology through the transfer of information from a low-power, longer-wavelength beam to one of a higher power and shorter wavelength.

## ACKNOWLEDGMENTS

We acknowledge funding from the UK National Quantum Hub for Imaging (QUANTIC, No. EP/T00097X/1),

an EPSRC DTP, and the Royal Society (No. UF160475).

- [1] X. Y. Zou, L. J. Wang, and L. Mandel, Induced Coherence and Indistinguishability in Optical Interference, *Phys. Rev. Lett.* **67**, 318 (1991).
- [2] A. Hochrainer, M. Lahiri, M. Erhard, M. Krenn, and A. Zeilinger, Quantum indistinguishability by path identity and with undetected photons, *Rev. Mod. Phys.* **94**, 025007 (2022).
- [3] S. P. Kulik, G. A. Maslennikov, S. P. Merkulova, A. N. Penin, L. K. Radchenko, and V. N. Krasheninnikov, Two-photon interference in the presence of absorption, *J. Exp. Theor. Phys.* **98**, 31 (2004).
- [4] G. B. Lemos, V. Borish, G. D. Cole, S. Ramelow, R. Lapkiewicz, and A. Zeilinger, Quantum imaging with undetected photons, *Nature* **512**, 409 (2014).
- [5] A. Barh, C. Pedersen, L. Meng, P. Tidemand-Lichtenberg, and P. J. Rodrigo, Parametric upconversion imaging and its applications, *Adv. Opt. Photon.* **11**, 952 (2019).
- [6] L. M. Kehlet, P. Tidemand-Lichtenberg, J. S. Dam, and C. Pedersen, Infrared upconversion hyperspectral imaging, *Opt. Lett.* **40**, 938 (2015).
- [7] R. S. Aspden, N. R. Gemmill, P. A. Morris, D. S. Tasca, L. Mertens, M. G. Tanner, R. A. Kirkwood, A. Ruggeri, A. Tosi, R. W. Boyd, G. S. Buller, R. H. Hadfield, and M. J. Padgett, Photon-sparse microscopy: Visible light imaging using infrared illumination, *Optica* **2**, 1049 (2015).
- [8] K. W. C. Chan, M. N. O’Sullivan, and R. W. Boyd, Two-color ghost imaging, *Phys. Rev. A* **79**, 033808 (2009).
- [9] M. G. Basset, A. Hochrainer, S. Töpfer, F. Rieinger, P. Bickert, J. R. León-Torres, F. Steinlechner, and M. Gräfe, Video-rate imaging with undetected photons, *Laser Photon. Rev.* **15**, 2000327 (2021).

- [10] S. Töpfer, M. G. Basset, J. Fuenzalida, F. Steinlechner, J. P. Torres, and M. Gräfe, Quantum holography with undetected light, *Sci. Adv.* **8**, eabl4301 (2022).
- [11] I. Kviatkovsky, H. M. Chrzanowski, E. G. Avery, H. Bartolomaeus, and S. Ramelow, Microscopy with undetected photons in the mid-infrared, *Sci. Adv.* **6**, 264 (2020).
- [12] A. V. Paterova, H. Yang, C. An, D. A. Kalashnikov, and L. A. Krivitsky, Tunable optical coherence tomography in the infrared range using visible photons, *Quantum Sci. Technol.* **3**, 025008 (2018).
- [13] C. Lindner, F. Kühnemann, J. Kiessling, and S. Wolf, Fourier transform infrared spectroscopy with visible light, *Opt. Express* **28**, 4426 (2020).
- [14] M. Arahata, Y. Mukai, T. Tashima, R. Okamoto, and S. Takeuchi, Wavelength-Tunable Quantum Absorption Spectroscopy in the Broadband Midinfrared Region, *Phys. Rev. Appl.* **18**, 034015 (2022).
- [15] A. Rojas-Santana, G. J. Machado, M. V. Chekhova, D. Lopez-Mago, and J. P. Torres, Analysis of the signal measured in spectral-domain optical coherence tomography based on nonlinear interferometers, *Phys. Rev. A* **106**, 033702 (2022).
- [16] A. Vanselow, P. Kaufmann, I. Zorin, B. Heise, H. M. Chrzanowski, and S. Ramelow, Frequency-domain optical coherence tomography with undetected mid-infrared photons, *Optica* **7**, 1729 (2020).
- [17] G. J. Machado, G. Frascella, J. P. Torres, and M. V. Chekhova, Optical coherence tomography with a nonlinear interferometer in the high parametric gain regime, *Appl. Phys. Lett.* **117**, 094002 (2020).
- [18] Y. Mukai, M. Arahata, T. Tashima, R. Okamoto, and S. Takeuchi, Quantum Fourier-Transform Infrared Spectroscopy for Complex Transmittance Measurements, *Phys. Rev. Appl.* **15**, 034019 (2021).
- [19] A. C. Cardoso, L. P. Berrueto, D. F. Ávila, G. B. Lemos, W. M. Pimenta, C. H. Monken, P. L. Saldanha, and S. Pádua, Classical imaging with undetected light, *Phys. Rev. A* **97**, 033827 (2018).
- [20] Y. Michael, I. Jonas, L. Bello, M.-E. Meller, E. Cohen, M. Rosenbluh, and A. Pe'er, Augmenting the Sensing Performance of Entangled Photon Pairs through Asymmetry, *Phys. Rev. Lett.* **127**, 173603 (2021).
- [21] P. Vergyris, C. Babin, R. Nold, E. Gouzien, H. Herrmann, C. Silberhorn, O. Alibert, S. Tanzilli, and F. Kaiser, Two-photon phase-sensing with single-photon detection, *Appl. Phys. Lett.* **117**, 024001 (2020).
- [22] D. A. Kalashnikov, A. V. Paterova, S. P. Kulik, and L. A. Krivitsky, Infrared spectroscopy with visible light, *Nat. Photon.* **10**, 98 (2016).
- [23] S. K. Lee, T. H. Yoon, and M. Cho, Interferometric quantum spectroscopy with undetected photons via distinguishability modulation, *Opt. Express* **27**, 14853 (2019).
- [24] A. Buzas, E. K. Wolff, M. G. Benedict, P. Ormos, and A. Der, Biological microscopy with undetected photons, *IEEE Access* **8**, 107539 (2020).
- [25] M. I. Kolobov, E. Giese, S. Lemieux, R. Fickler, and R. W. Boyd, Controlling induced coherence for quantum imaging, *J. Opt.* **19**, 054003 (2017).
- [26] E. Giese, S. Lemieux, M. Manceau, R. Fickler, and R. W. Boyd, Phase sensitivity of gain-unbalanced nonlinear interferometers, *Phys. Rev. A* **96**, 053863 (2017).
- [27] J. Flórez, J. S. Lundeen, and M. V. Chekhova, Pump depletion in parametric down-conversion with low pump energies, *Opt. Lett.* **45**, 4264 (2020).
- [28] A. G. White, J. R. Mitchell, O. Nairz, and P. G. Kwiat, “Interaction-free” imaging, *Phys. Rev. A* **58**, 605 (1998).
- [29] A. C. Elitzur and L. Vaidman, Quantum mechanical interaction-free measurements, *Found. Phys.* **23**, 987 (1993).
- [30] M. Manceau, G. Leuchs, F. Khalili, and M. Chekhova, Detection Loss Tolerant Supersensitive Phase Measurement with an SU(1,1) Interferometer, *Phys. Rev. Lett.* **119**, 223604 (2017).
- [31] J. Fuenzalida, A. Hochrainer, G. B. Lemos, E. A. Ortega, R. Lapkiewicz, M. Lahiri, and A. Zeilinger, Resolution of quantum imaging with undetected photons, *Quantum* **6**, 646 (2022).
- [32] B. Viswanathan, G. B. Lemos, and M. Lahiri, Resolution limit in quantum imaging with undetected photons using position correlations, *Opt. Express* **29**, 38185 (2021).
- [33] A. Vega, E. A. Santos, J. Fuenzalida, M. G. Basset, T. Pertsch, M. Gräfe, S. Saravi, and F. Setzpfandt, Fundamental resolution limit of quantum imaging with undetected photons, *Phys. Rev. Res.* **4**, 033252 (2022).
- [34] M. Widarsson, M. Henriksson, L. Barrett, V. Pasiskevicius, and F. Laurell, Room temperature photon-counting lidar at 3  $\mu\text{m}$ , *Appl. Opt.* **61**, 884 (2022).
- [35] G. G. Taylor, D. Morozov, N. R. Gemmell, K. Erotokritou, S. Miki, H. Terai, and R. H. Hadfield, Photon counting lidar at 2.3  $\mu\text{m}$  wavelength with superconducting nanowires, *Opt. Express* **27**, 38147 (2019).
- [36] V. Verma, B. Korzh, A. B. Walter, A. E. Lita, R. M. Briggs, M. Colangelo, Y. Zhai, E. E. Wollman, A. D. Beyer, and J. P. Allmaras, *et al.*, Single-photon detection in the mid-infrared up to 10  $\mu\text{m}$  wavelength using tungsten silicide superconducting nanowire detectors, *APL Photon.* **6**, 056101 (2021).
- [37] J. A. Lau, V. B. Verma, D. Schwarzer, and A. M. Wodtke, Superconducting single-photon detectors in the mid-infrared for physical chemistry and spectroscopy, *Chem. Soc. Rev.* **52**, 921 (2023).
- [38] A. P. Demchenko, Photobleaching of organic fluorophores: Quantitative characterization, mechanisms, protection, *Methods Appl. Fluoresc.* **8**, 022001 (2020).
- [39] C. Sandt and F. Borondics, Super-resolution infrared microspectroscopy reveals heterogeneous distribution of photosensitive lipids in human hair medulla, *Talanta* **254**, 124152 (2023).
- [40] K. L. Tosheva, Y. Yuan, P. M. Pereira, S. Culley, and R. Henriques, Between life and death: Strategies to reduce phototoxicity in super-resolution microscopy, *J. Phys. D: Appl. Phys.* **53**, 163001 (2020).
- [41] S. I. Firth, C.-T. Wang, and M. B. Feller, Retinal waves: Mechanisms and function in visual system development, *Cell Calcium* **37**, 425 (2005).